Opto-Electronic Advances

ISSN 2096-4579 CN 51-1781/TN

Stimulated Raman scattering microscopy with phase-controlled light focusing and aberration correction for rapid and label-free, volumetric deep tissue imaging

Weiqi Wang and Zhiwei Huang

Citation: Wang WQ, Huang ZW. Stimulated Raman scattering microscopy with phase-controlled light focusing and aberration correction for rapid and label-free, volumetric deep tissue imaging. *Opto-Electron Adv* **7**, 240064(2024).

https://doi.org/10.29026/oea.2024.240064

Received: 22 March 2024; Accepted: 3 June 2024; Published online: 17 July 2024

Opto-Electronic Advances

Article

August 2024, Vol. 7, No. 8

DOI: 10.29026/oea.2024.240064

Stimulated Raman scattering microscopy with phase-controlled light focusing and aberration correction for rapid and label-free, volumetric deep tissue imaging

Weiqi Wang[1] and Zhiwei Huang[1*]

We report a novel stimulated Raman scattering (SRS) microscopy technique featuring phase-controlled light focusing and aberration corrections for rapid, deep tissue 3D chemical imaging with subcellular resolution. To accomplish phase-controlled SRS (PC-SRS), we utilize a single spatial light modulator to electronically tune the axial positioning of both the shortened-length Bessel pump and the focused Gaussian Stokes beams, enabling *z*-scanning-free optical sectioning in the sample. By incorporating Zernike polynomials into the phase patterns, we simultaneously correct the system aberrations at two separate wavelengths (~240 nm difference), achieving a ~3-fold enhancement in signal-to-noise ratio over the uncorrected imaging system. PC-SRS provides >2-fold improvement in imaging depth in various samples (e.g., polystyrene bead phantoms, porcine brain tissue) as well as achieves SRS 3D imaging speed of ~13 Hz per volume for real-time monitoring of Brownian motion of polymer beads in water, superior to conventional point-scanning SRS 3D imaging. We further utilize PC-SRS to observe the metabolic activities of the entire tumor liver in living zebrafish in cell-silent region, unraveling the upregulated metabolism in liver tumor compared to normal liver. This work shows that PC-SRS provides unprecedented insights into morpho-chemistry, metabolic and dynamic functioning of live cells and tissue in real-time at the subcellular level.

Keywords: SRS 3D imaging; phase-controlled light focusing; image aberration corrections; deep tissue imaging

Wang WQ, Huang ZW. Stimulated Raman scattering microscopy with phase-controlled light focusing and aberration correction for rapid and label-free, volumetric deep tissue imaging. *Opto-Electron Adv* **7**, 240064 (2024).

Introduction

Coherent Raman scattering (CRS) microscopy (e.g., coherent anti-Stokes Raman scattering (CARS), and stimulated Raman scattering (SRS) microscopy) has emerged as an attractive label-free vibrational spectroscopic imaging tool to study the complex structures and molecular conformations of cells and tissue in biological and biomedical systems (e.g., cancer diagnosis and characterization, tumor metabolisms, drug deliveries and pharmacodynamics, molecular genetics, organ functions, and developmental biology, etc.[1–6]). Unlike traditional fluorescence imaging methods that often require fluorescent labels to visualize specific organelles within cells and tissues[7], CRS microscopy relies on the intrinsic vibrational properties of molecules to generate biochemical contrast in tissue and cells imaging[8,9]. This allows for the

[1]Optical Bioimaging Laboratory, Department of Biomedical Engineering, College of Design and Engineering, National University of Singapore, Singapore 117576.

*Correspondence: ZW Huang, E-mail: biehzw@nus.edu.sg

Received: 22 March 2024; Accepted: 3 June 2024; Published online: 17 July 2024

label-free imaging of biological specimens, providing new insights into their biochemical structure and dynamics in a non-invasive manner. In the realm of CRS microscopy, CARS microscopy is first developed for label-free biomolecular imaging in biological and biomedical systems, but hampered by the distorted Raman spectrum and limited detection sensitivity due to the strong non-resonant background interference[10,11]. SRS microscopy possesses the capability to probe the molecular vibrations of biochemical constituents in tissue and cells without non-resonant background interference, enabling quantitative biochemical imaging of the samples in various applications. In conventional SRS (C-SRS) imaging, two ultrafast near-infrared (NIR) laser beams (i.e., pump, $\omega_{\rm P}$, and Stokes, $\omega_{\rm S}$) are temporally and spatially overlapped and focused onto a sample. When the frequency difference between the two lasers matches the vibrational frequency of target molecules (i.e., $\omega = \omega_{\rm P} - \omega_{\rm S}$), coherent Raman scattering process will occur along the phase-matching direction, empowering SRS imaging with biomolecular contrast[10].

Current C-SRS microscopy imaging technique mainly focuses on 2D imaging of biomolecules (primarily lipids and proteins) with strong Raman peaks in the high wavenumber region. To obtain more comprehensive 3D biochemical information, a series of 2D images are captured by moving either the objective lens or the sample stage along the *z*-axis for co-registration and reconstruction of the 3D structure of tissue and cells[12]. However, this mechanical *z*-scanning is prone to artifacts and co-registration errors, affecting 3D image quality and speed[13]. The strong light scattering effect in turbid media (e.g., biotissue) also hinders the penetration of incident laser beams into bulky tissue, leading to the reduced signal and imaging depth in deeper tissue regions[14]. To address these limitations, non-mechanical *z*-scanning volumetric imaging techniques (e.g., optical projection tomography (OPT)[15] and optical beating tomography (OBT)[16]) have been explored for SRS 3D imaging by utilizing scattering-resilient Bessel beams. However, the extended length of the Bessel beam significantly reduces the local laser intensity, limiting the signal-to-noise ratio (SNR) of SRS signals for rapid SRS 3D imaging. Consequently, these techniques are primarily applied to the 3D imaging in the high wavenumber region. The imaging process also becomes time-consuming due to a constrained SNR, necessitating several to dozens of minutes per volume for biological applications[15,16].

In this work, we develop a unique phase-controlled SRS microscopy (PC-SRS) technique for z-scanning-free, deep tissue 3D chemical imaging within both cell-silent and high wavenumber regions. In PC-SRS, a spatial light modulator (SLM) is used to electronically manipulate the axial positioning of both the shortened-length Bessel pump beam and the focused Gaussian Stokes beam in the sample for SRS 3D imaging. In parallel, Zernike polynomials (ZPs) are utilized in PC-SRS to correct the system aberrations by projecting both the correction and modulation phase patterns onto the same SLM. We have derived and analyzed the working principle of PC-SRS method theoretically and also built the PC-SRS imaging system to experimentally demonstrate its utility for rapid and label-free volumetric chemical imaging in a variety of samples (e.g., Brownian motion of polymer beads in water, polystyrene (PS) beads phantom, and porcine brain tissue). We have also applied PC-SRS to visualize the metabolic activity differences between tumor and normal liver tissue in live zebrafish by monitoring the newly synthesized C-D bonds in cell-silent regions, showcasing the superiority of PC-SRS imaging in biological and biomedical applications.

Methods and materials

Principle of the PC-SRS technique

In C-SRS imaging, the sample is illuminated by the collinear pump and Stokes beams under a tight focus through a high numerical aperture (N.A.) of objective lens. The SRS signal generated is proportional to the product of the pump and Stokes beam intensities[10]. But in PC-SRS, the pump light is converted into a ring-shaped beam by using a pair of axicons, in which the electric field of the ring pump beam is expressed[15]:

$$E_{\rm pR}(r,z) = E_{\rm p0}\frac{\omega_{\rm p0}}{\omega(z)}{\rm e}^{-\frac{r^2}{\omega^2(z)}}{\rm e}^{{\rm i}\varphi(r,z)}{\rm rect}(r-r_{\rm R}), \quad (1)$$

where $E_{\rm pR}(r, z)$ is the electric field distribution of the ring pump beam. r and z are the coordinates in the lateral and longitudinal directions, respectively. $E_{\rm p0}$ is the electric field amplitude of the incident Gaussian pump beam with beam waist $\omega_{\rm p0}$. $\omega(z)$ is the beam waist at position z. $r_{\rm R}$ is the radius of ring-shaped pump beam.

The ring shape is modeled by a rectangle function:

$${\rm rect}(r-r_{\rm R}) = \begin{cases} 1, |r-r_{\rm R}| \le \dfrac{d}{2} \\ 0, |r-r_{\rm R}| > \dfrac{d}{2} \end{cases}, \quad (2)$$

where d is the width of the ring.

The ring-shaped pump beam is modulated by SLM to control the axial position of the focused pump beam after passing through the objective lens. In practice, we modify the divergence angle of the incident ring-shaped pump beam at the Fourier plane of the imaging system by varying the phase patterns using an SLM. The optical pathlength difference (OPD) between the incident plane wave and the spherical wavefront is calculated to determine the axial position of the focal spot away from the focal plane of the lens. Based on the Gaussian thin lens formula[17], the relationship between the axial position of the incident point source and the focus is as follows:

$$\frac{1}{l}+\frac{1}{\Delta z+f_0}=\frac{1}{f_0}, \tag{3}$$

where f_0 is the focal length of the objective lens, l is the distance of the point source away from the lens, and Δz is the displacement of the focal spot from the focus of the lens. As such, OPD between the spherical and the plane wavefront can be calculated:

$$OPD=(l-f_0)-\sqrt{(l-f_0)^2-r_F^2}\,, \tag{4}$$

where r_{F} is the radial coordinate on the Fourier plane. Under the paraxial condition, we can make Taylor expansion in Eq. (4) to obtain the relationship between the modulation phase Δp_{SLM} (OPD multiplied by wavevector k) and the Δz, i.e.,

$$\Delta p_{\mathrm{SLM}}=\frac{k\Delta z}{2f_0^2}r_{\mathrm{F}}^2\,, \tag{5}$$

where $r_{\mathrm{F}}=\sqrt{x^2+y^2}$, x and y are the Cartesian coordinates on the Fourier plane (i.e., SLM). The modulation phase Δp_{SLM} can be transformed into a digital phase image using MATLAB, where the pixel resolution of this phase image is set to match the pixel number of SLM (1920×1200) used in our setup. The phase image is then projected onto the SLM to modulate the incident ring-shaped pump beam, where the electric field distribution after modualtion for the pump beam can be expressed:

$$E_{\mathrm{pR-SLM}}=E_{\mathrm{pR}}(r,z)\,e^{\mathrm{i}\Delta p_{\mathrm{SLM}}}. \tag{6}$$

The electric field distribution after passing through the objective lens can be modeled by using the Fourier-Bessel transform[18]:

$$E_{\mathrm{p}}(r,z')=E_{\mathrm{p0}}\frac{\omega_{\mathrm{p0}}}{\omega(z')}\mathrm{e}^{-\frac{r_{\mathrm{R}}^2}{\omega^2(z')}}\left(-\mathrm{i}\frac{kr_{\mathrm{R}}d}{f_0}\right)J_0\left(\frac{kr_{\mathrm{R}}}{f_{\mathrm{o}}}r\right)\mathrm{e}^{\mathrm{i}\varphi(r,z')}, \tag{7}$$

where $z'=z+\frac{r_{\mathrm{F}}^2\Delta z}{2f_0^2}$. J_0 is the zeroth-order Bessel function of the first kind. $\omega(z')=\omega_{\mathrm{p0}}\sqrt{1+\left(\frac{z'}{z_{\mathrm{B}}}\right)^2}$, z_{B} is the equivalent Rayleigh range of the generated Bessel beam[15]. Hence, the intensity distribution of the pump beam in the sample space can be written:

$$I_{\mathrm{p}}(r,z')=I_{\mathrm{p0}}\frac{\omega_{\mathrm{p0}}^2}{\omega^2(z')}\mathrm{e}^{-\frac{2r_{\mathrm{R}}^2}{\omega^2(z')}}\left(\frac{kr_{\mathrm{R}}\mathrm{d}}{f_0}\right)^2\mathrm{J}_0^2\left(\frac{kr_{\mathrm{R}}}{f_0}r\right), \tag{8}$$

where I_{p0} is the intensity of the incident pump beam. From Eq. (8), we can find the ring-shaped pump beam is formed as a Bessel beam after passing through the objective lens and focused into the sample. The depth-of-focus (DOF) of the Bessel pump beam is[19]:

$$DOF=\frac{2.8f_0^2}{kr_{\mathrm{R}}d}\,. \tag{9}$$

According to Eq. (9), the length of the Bessel pump beam in the sample can be tailored for shortening to increase the local excitation power density through adjusting the diameter and width of the ring-shaped pump beam, which is achieved by manipulating the diameter of the incident Gaussian beam and/or adjusting the distance between the two axicons used in the current experiments. Meanwhile, the Gaussian Stokes beam is also modulated by the same SLM and focused onto the sample as an Airy spot under the high NA objective lens, in which the intensity distribution in the sample space is $I_{\mathrm{S}}(r,z')=I_{\mathrm{S0}}\exp\left(\frac{-2r^2}{\omega_{\mathrm{S}}(z')^2}\right)$, where I_{S0} is the on-axis intensity of the incident Gaussian Stokes beam and ω_{S} is the waist of the Stokes beam. Therefore, the SRS intensity generated from the sample can be expressed as:

$$I_{\mathrm{SRS}}(r,z')=C_0\mathrm{Im}\left(\chi^{(3)}\right)I_{\mathrm{p}}(r,z')I_{\mathrm{S}}(r,z')\,. \tag{10}$$

Equation (10) serves as the foundation in PC-SRS microscopy for z-scanning-free SRS 3D imaging in tissue and cells.

PC-SRS imaging system

Figure 1(a) depicts the schematic of the PC-SRS imaging system developed for 3D chemical imaging. A 100-fs laser with 80 MHz repetition rates (InSight, Spectra Physics) provides dual-color laser outputs: one is a 1041 nm laser beam (Stokes), and the other is a tunable beam (pump) ranging from 680 to 1300 nm for SRS excitation. For the pump optical path, the beam is converted into a ring-shaped beam using a pair of 1° axicons (AX251-B, Thorlabs Inc.). The Stokes beam is modulated at 20 MHz using an electro-optical modulator (EOM) and then

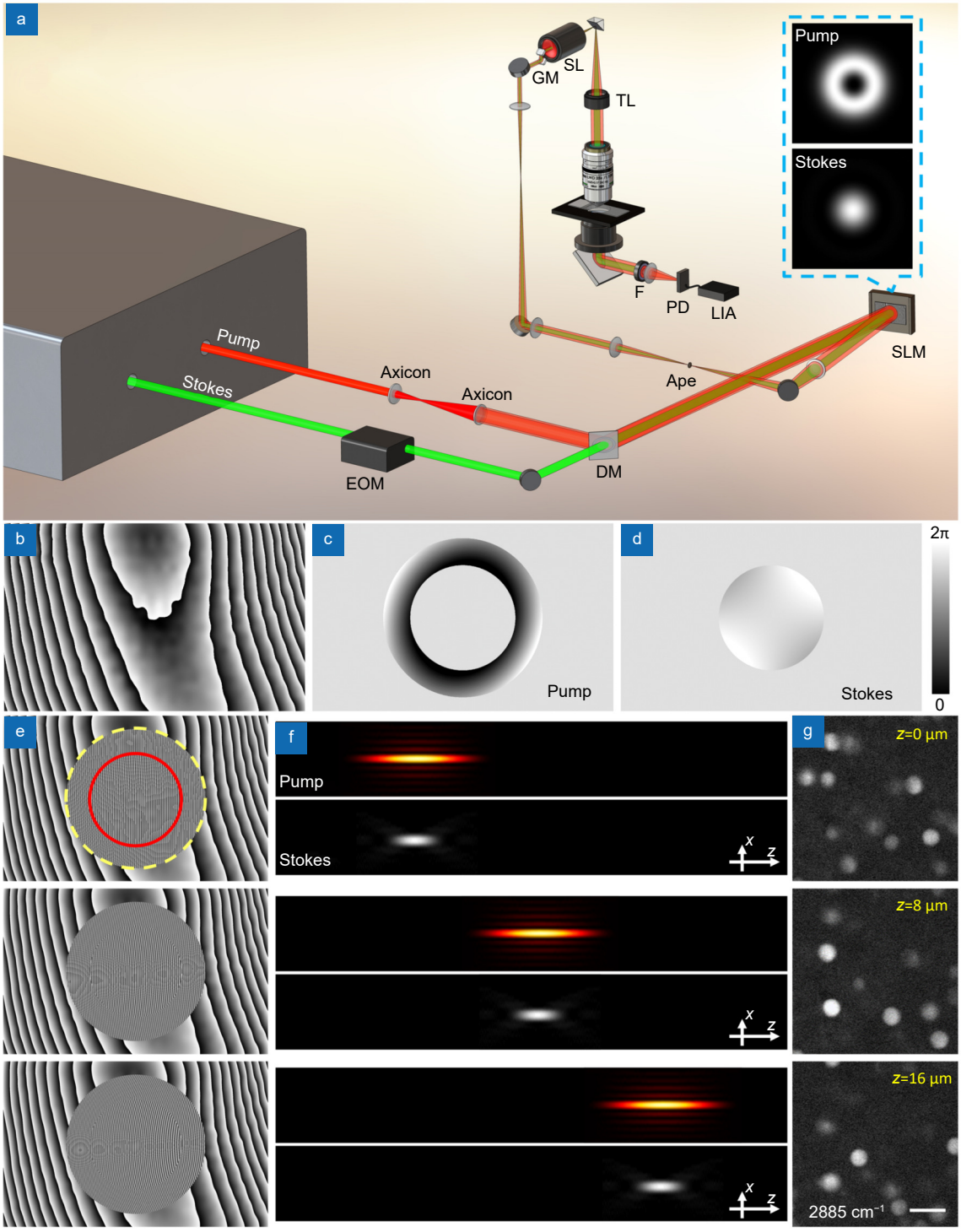

Fig. 1 | (**a**) Schematic of the PC-SRS microscope system for 3D chemical imaging. EOM, electro-optical modulator; DM, dichroic mirror; SLM, spatial light modulator; Ape, aperture; GM, galvo mirror; SL, scan lens; TL, tube lens; F, filter; PD, photodiode; LIA, lock-in amplifier. Inset drawings illustrate the ring-shaped pump beam and Gaussian Stokes beam on the SLM. (**b**) The distortion-corrected phase pattern for the SLM. (**c**, **d**) The phase patterns mimicking the ZPs for pump and Stokes beams, respectively, which are incorporated into (b) to correct system aberrations. (**e**) The phase patterns used in experiments to control the axial positionings of the Bessel pump and Gaussian Stokes beams in the sample. The region enclosed by the solid red circle is designated for the Stokes beam, and the area between the solid red and yellow dashed circles is for the pump beam. (**f**) The schematic of the generated shortened-length Bessel pump beam and Gaussian Stokes beam at different depths corresponding to the phase patterns in (e). (**g**) Raw SRS images of 10 μm PS beads (2885 cm^{-1} of CH_2 asymmetric stretching) acquired by PC-SRS at z=0 μm, 8 μm, and 16 μm, respectively. Scale bar: 20 μm.

combined with the ring-shaped pump beam by a dichroic mirror (NFD01-1040-25×36, Semrock, Inc.). Both laser beams are projected onto the SLM (SLM-200, Santec, Inc.) and modulated at different regions on the SLM plane (see the inset drawing of the pump and Stokes beams in Fig. 1(a)), effectively avoiding the dispersion effect caused by the SLM. After modulation by the SLM, the +1 order of the diffracted pump and Stokes light is selected for SRS imaging, while other orders of diffracted beams are blocked by an aperture. The pump and Stokes beams are finally coupled into a laser-scanning microscope (MPM-4R, Thorlabs Inc.) with a galvo-scanner (GVSM002, Thorlabs Inc.), and focused onto the sample with a high-NA objective lens (CFI75 APOCHROMAT 25XW MP 1300, *NA*=1.1, Nikon). A high-NA condenser (CC Achromat/Aplanat, *NA*=1.4, Nikon) is used to collect the forward SRS emission from the sample. In the detection path, the Stokes beam is spectrally removed using a set of bandpass filters (795/75, Semrock), while the de-modulated pump beam is detected through a large-area photodiode with a lock-in amplifier for SRS 3D imaging.

Figure 1(b) shows the phase patterns used to eliminate the wavefront distortion induced by the SLM device. Figure 1(c, d) present the phase patterns mimicking the ZPs to correct the aberrations in the pump and Stokes beams, respectively (details refer to Supplementary Material 1, Fig. S1). The phase patterns in (c-d) are both incorporated into (b), and then projected onto the SLM for aberration-corrected SRS imaging. Figure 1(e) shows the phase patterns used in the PC-SRS imaging system, which consist of the aberration-corrected phase patterns (Fig. 1(b–d)) and the depth modulation phase patterns. The phase pattern within the ring area (encircled by a dashed yellow and a solid red circle) is designated for modulating the ring-shaped pump beam. The pattern inside the solid red circle is specifically employed for modulating the Stokes beam. The depth modulation phase patterns in PC-SRS are designed to provide an optical pathlength difference at each point on the wavefront at the Fourier plane of the system, leading to a variation of divergent angles of the incident pump and Stokes beams. Figure 1(f) illustrates the working principle of the PC-SRS technique, where the axial positions of both the shortened-length Bessel pump beam and the Gaussian Stokes spot can be manipulated along the z-axis by controlling the divergent angles of the incident beams with the SLM before they enter the objective lens (details refer to Supplementary information, Fig. S2). The modulated phase patterns corresponding to the specific depths (Eq. (5)) are generated and varied on the SLM for rapid and deep 3D chemical imaging. For example, Fig. 1(g) displays the raw SRS images of PS beads captured at depths of z=0 μm, 8 μm, and 16 μm, respectively, proving the precise depth-sectioning ability of PC-SRS experimentally.

Sample preparations

The 10 μm PS beads (17136, Polysciences Inc.) are embedded in 2% agarose gel phantoms (~2×10^7 particles/mL) for SRS 3D imaging (note that the scattering coefficients of the PS beads phantom are estimated to be ~33.5 cm^{-1} at 800 nm and ~28.6 cm^{-1} at 1041 nm based on Mie scattering model[20]). A suspension of 4.5 μm PS beads (17135, Polysciences Inc., diluted 10 times in water) is dropped onto microscope slides with a single well (MS15C1, Thorlabs) for SRS monitoring of Brownian motion in water. The 500 nm PS beads (07307, Polysciences Inc.) and 1 μm PMMA beads (07307, Polysciences Inc.) are fixed on microscope slides for assessing the point spread function (PSF) and SNR improvement in PC-SRS microscopy, respectively. The 500 nm fluorescent beads (15700-1, Polysciences, Inc.) are fixed on microscope slides for measuring the intensity distribution of the Bessel pump beam in the x-z plane. Dimethyl sulfoxide (DMSO) is diluted to concentrations of 0.14 M, 0.35 M, 0.7 M, and 1.4 M in water, respectively, and sandwiched in 170 μm-thick chamber to examine the SRS detection limit. Fresh porcine brain tissue samples (purchased from a local supermarket) are sectioned into a thickness of ~510 μm and placed on the microscope slides for SRS 3D tissue imaging.

Zebrafish model preparations for metabolism visulizaiton in tumor and normal liver by PC-SRS

Deuterium oxide (D_2O) can be used as a universal metabolic probe by tracking the formation of C–D bonds in macromolecules synthesized during cellular metabolic activities[2]. In our experiments, 40% D_2O (151882 10X0.6ML, Sigma) aqueous solution is used to feed zebrafish with tumor and normal liver from 3-day post-fertilization (dpf) onwards[21,22]. The zebrafish larvae are anaesthetized in 80 mg/L MS-222 for about 1 minute and then immobilized with 3% methylcellulose for PC-SRS imaging from 6 dpf to 11 dpf. At least three zebrafish for each condition are imaged on each dpf in Figs. 4 and 5.

Imaging parameters

A time constant of 2 μs is set in lock-in amplifier for SRS imaging. A series of 2D images with 256 × 256 pixels are acquired by PC-SRS imaging at a raster scan rate of 0.6 Hz or 6 Hz (pixel dwell time of 10 μs or 1 μs) for CD (2186 cm^{-1}) and CH chemical bonds. For Brownian motion measurements, the 2D raster scan rate is set at 51.2 Hz (pixel dwell time of 2.8 μs; 64 × 64 pixels). In SRS 3D imaging, the Stokes beam is fixed at 1041 nm, while the wavelengths of the pump beam are set at 797 nm, 804 nm, and 848 nm, respectively, to acquire SRS images at 2935 cm^{-1} (CH_3 stretching of lipids and proteins), 2845 cm^{-1} (CH_2 symmetric stretching of lipids), and 2186 cm^{-1} (CD bond), accordingly. The signal intensity ratio at 2935 cm^{-1} and 2845 cm^{-1} is estimated to be 0.9:1 after SRS system calibration with Rhodamine 6G[1]. The SRS image of proteins is obtained by normalizing the SRS image at 2935 cm^{-1} with a factor of 0.9 and subtracted to the SRS image at 2845 cm^{-1}. Other specific imaging parameters, such as the average laser powers on the samples, total imaging time, and the number of 2D images for 3D volume reconstruction, are indicated in the corresponding figure legends.

3D image acquisition and reconstruction

For rapid SRS 3D imaging, the SLM is triggered and synchronized with the microscope scanning module in PC-SRS. The generated phase patterns (Fig. 1(e)) are projected onto the SLM (operating at a 60 Hz refresh rate) to acquire 2D images across the corresponding tissue depths. By varying the phase patterns on the SLM, a series of 2D images are obtained, which are then used to reconstruct a 3D volume in PC-SRS. Each phase pattern corresponds to a 2D image from a specific depth. Hence, the number of phase patterns used in each SRS measurement corresponds to the number of 2D images required for 3D reconstruction. To compare the penetration depth between PC-SRS and C-SRS microscopy, the system aberrations are corrected for both techniques. In C-SRS, the pump and Stokes beams are directed to different areas of the SLM, each with corresponding aberration-corrected phase patterns. After passing through the objective lens, the Gaussian pump and Stokes foci are overlapped in the sample. The C-SRS 3D volume is then acquired using a motorized translation stage (with a switching rate of 10 Hz, KVS30, Thorlabs) to move the sample stage incrementally along the *z*-axis.

Estimations of spatial resolution and light penetration depth by PC-SRS

The lateral resolution of PC-SRS can be estimated using the formula $1/\sqrt{1/(\beta)^2+1/(\sigma_S)^2}$ [23], where the PSF (main lobe) of the Bessel pump beam is calculated by $\beta=\frac{0.38\lambda_p}{NA_p}$ [24]. Here, λ_p represents the wavelength of the pump beam, and NA_p is the numerical aperture of the ring-shaped pump beam. The PSF of Gaussian Stokes beam is calculated by $\sigma_S=\frac{0.61\lambda_S}{NA_S}$, where λ_S is the wavelength of the Stokes beam, and NA_S is the numerical aperture of the Gaussian Stokes beam. With the use of λ_p =800 nm, λ_S =1041 nm and NA_p=0.52, NA_S=0.4 in this study, the lateral resolution of PC-SRS is calculated to be ~0.55 μm. In PC-SRS, the length of the Bessel pump beam is shortened, and its axial profile can be approximated by a Gaussian function. Therefore, the axial resolution of PC-SRS is calculated to be 5.4 μm using the formula $1/\sqrt{1/\left(\gamma_p\right)^2+1/\left(\gamma_S\right)^2}$ [23], where $\gamma_p=\frac{2\lambda_p}{NA_p^2}$ and $\gamma_S=\frac{2\lambda_S}{NA_S^2}$. The Gaussian function is employed to fit the intensity distribution of 500 nm PS beads (Fig. 2), where the full width at half maximum (FWHM) of the fit curve represents the resolution of the PC-SRS technique. The exponential decay function $I=I_0\exp(-\frac{z}{\delta})$ is used to estimate the penetration depth in tissue[23], where I_0 and I are the average SRS intensity at the surface (z=0) and the depth z, respectively. δ is the penetration depth, whereby the SRS intensity I is dropped by 1/e of the incident light intensity I_0.

Results

Performance of PC-SRS imaging system

Figure 2(a) displays the SRS image of 1 μm PMMA beads obtained by PC-SRS with the phase patterns in Fig. 1(b–d) for system aberration correction (AC-ON). In contrast, Fig. 2(b) presents the SRS image of the same PMMA beads by PC-SRS using only the phase pattern in Fig. 1(b), resulting in a significantly reduced SRS signal due to the absence of system aberration correction (AC-OFF). Figure 2(c) displays the comparison of intensity distributions of PMMA beads (indicated by yellow arrows) along the *x*-direction in (a) and (b), yielding a ~3-fold improvement in SRS generation with ZPs phase patterns in PC-SRS. Figure 2(d) depicts the SRS intensity versus DMSO concentrations measured by the PC-SRS

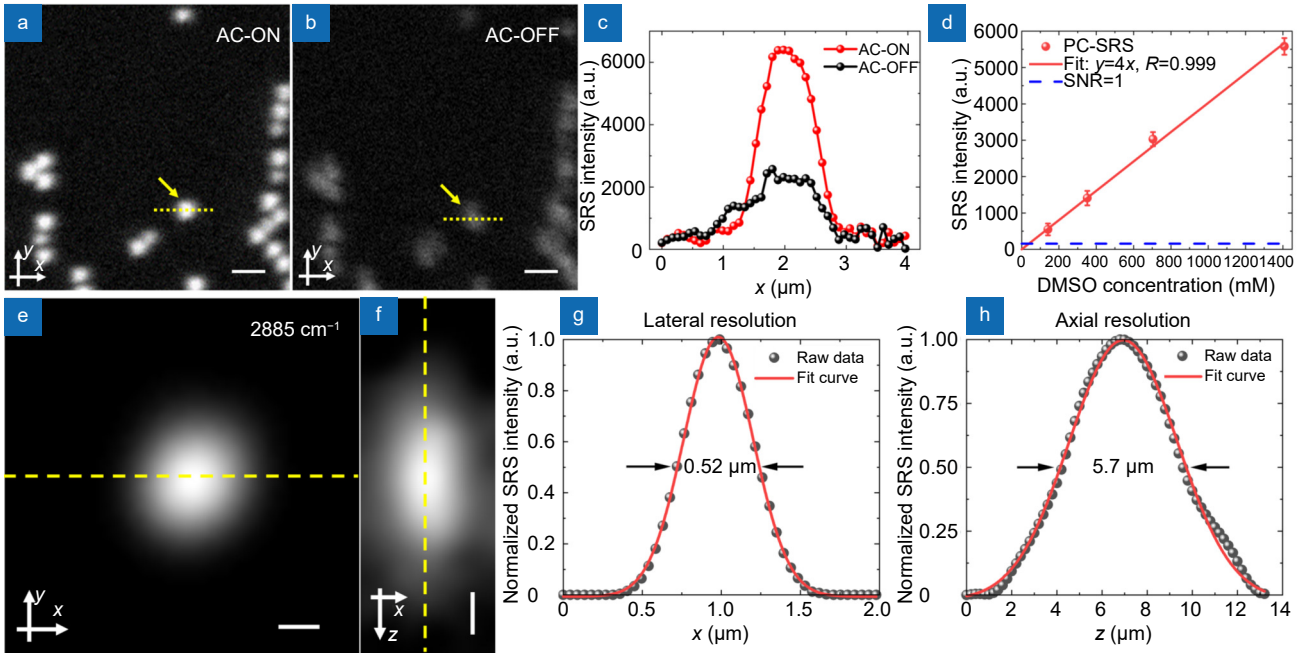

Fig. 2 | (**a**) SRS image (2885 cm^{-1} for CH_2 asymmetric stretching) of 1 μm PMMA beads using PC-SRS with AC-ON. Scale bar: 2 μm. (**b**) SRS image of the same PMMA beads using PC-SRS with AC-OFF. Scale bar: 2 μm. (**c**) SRS intensities of PMMA beads (indicated by yellow arrows) along the *x*-direction in (a) and (b). (**d**) The relationship between the SRS intensities and DMSO concentrations, where the detection limit of PC-SRS (39 mM, at SNR=1) is calculated with a linear fit curve. (**e**) SRS image (2885 cm^{-1}) of a 500 nm PS bead in the *x*-*y* plane using PC-SRS. Scale bar: 250 nm. (**f**) SRS image of the 500 nm PS bead in the *x*-*z* plane. Scale bar: 2 μm. The average powers of the pump and Stokes beams on the beads are 20 mW and 45 mW, respectively. (**g**–**h**) SRS intensity distributions along the *x*- and *z*-directions in (e) and (f), with the estimated FWHMs (lateral: 0.52 μm and axial: 5.7 μm) for PC-SRS.

technique. A linear relationship is observed, allowing for the quantitative SRS imaging of biochemicals in the sample. PC-SRS achieves a detection limit of ~39 mM (10 μs pixel dwell time at SNR=1, indicated by the dashed blue line in Fig. 2(d)), enabled by the utilization of ZPs and a shortened-length Bessel beam (4.73 μm in length, details refer to Supplementary information, Fig. S3) in SRS imaging. Figure 2(e, f) present the PSFs of a 500 nm PS bead captured by PC-SRS in the *x*-*y* and *x*-*z* planes, respectively. Figure 2(g, h) shows the lateral (0.52 μm) and axial (5.7 μm) resolutions of the PC-SRS imaging technique by calculating the FWHMs along the *x*- and *z*- directions (Figure 2(e, f)). The measured spatial resolutions are in agreement with the theoretical calculations (refer to the section-Estimations of spatial resolution and light penetration depth by PC-SRS in Methods and Materials), confirming the subcellular-resolution imaging ability achieved by PC-SRS.

We also compare the light penetration depth of PC-SRS with C-SRS imaging by measuring SRS images of 10 μm PS beads in agarose gel phantoms (Fig. 3(a, b)). To mitigate the influence of NA differences on spatial resolution between the two imaging modalities, the same NAs for the pump (NA ~0.52) and Stokes (NA ~0.4) beams are used in both the PC-SRS and C-SRS techniques. The 3D distribution of PS beads in the gel phantom captured by PC-SRS imaging is almost identical to that obtained by C-SRS imaging, confirming the z-sectioning ability of PC-SRS without a need for mechanical z-scanning. Notably, the SRS signals of the PS beads in deeper phantom areas in PC-SRS are much stronger than those in C-SRS imaging (e.g., some beads as indicated by yellow arrows in Fig. 3(a) and 3(b)) due to the strong scattering effect encountered by the Gaussian pump beam used in C-SRS[25]. To quantitatively analyze the light penetration depth achieved by PC-SRS, Fig. 3(c) shows the normalized SRS intensity profiles of the beads versus depth z in PC-SRS compared to C-SRS imaging. Clearly, SRS intensity versus phantom depth in PC-SRS declines much slower than that in C-SRS imaging. The plots are fit with an exponential decay function (refer to *Spatial resolution and light penetration depth by PC-SRS in Methods and materials*). The penetration depth δ for PC-SRS is estimated to be ~124.4 μm (95% confidence interval: [82.61 μm, 166.2 μm]), while for C-SRS, δ is 65.4 μm (95% confidence interval: [43.2 μm, 87.56 μm]). Thus,

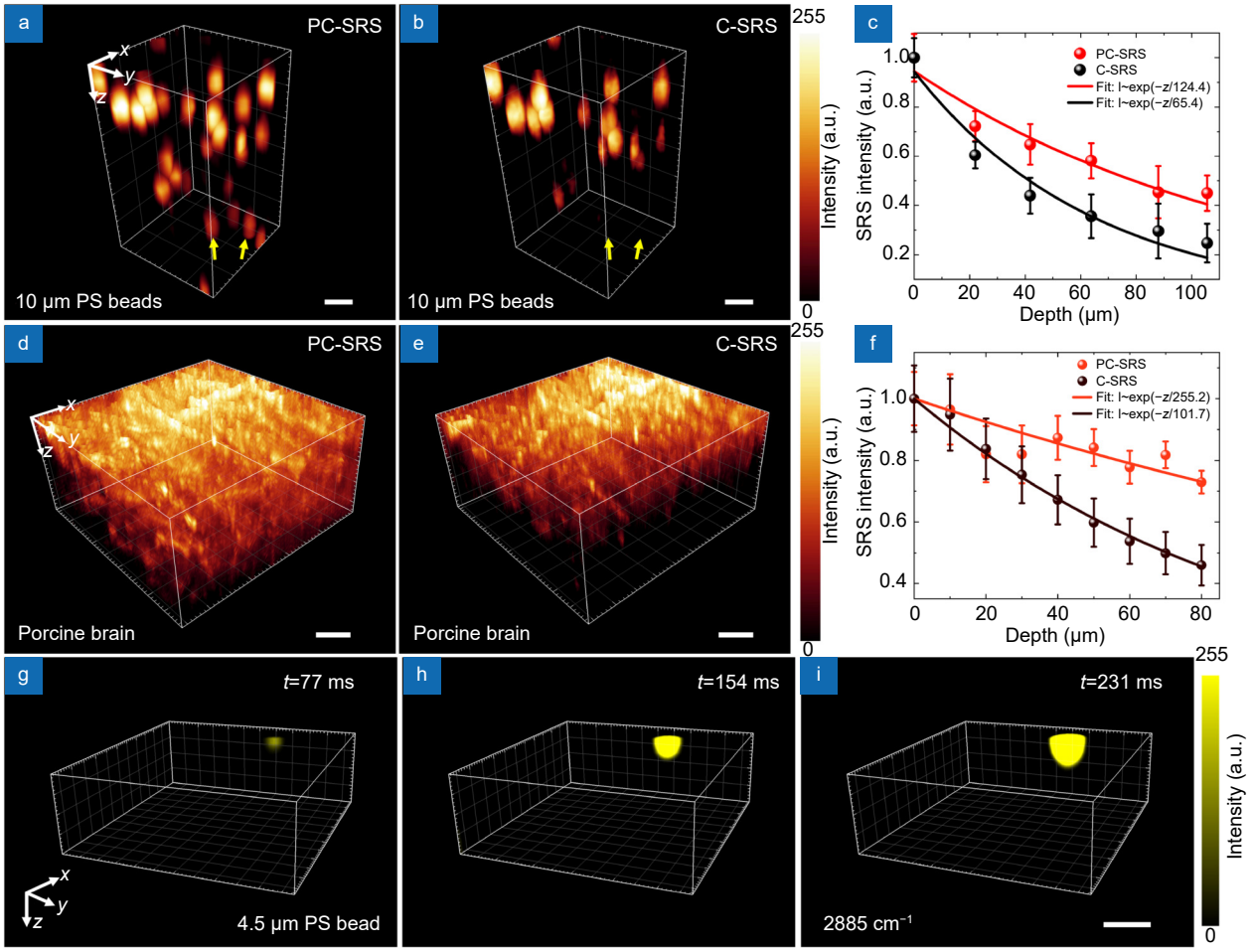

Fig. 3 | (**a**, **b**) SRS 3D images of 10 μm PS beads in a gel phantom (2885 cm^{-1}, CH_2 asymmetric stretching) using PC-SRS and C-SRS imaging. Yellow arrows highlight the brighter PS beads in deeper regions captured by PC-SRS. Image volume: 72 μm × 72 μm × 120 μm. Axial step size of 8.5 μm. A total of 14 depths are imaged with a 2.3 s acquisition time per 3D volume. Scale bar: 20 μm. (**c**) Comparison of normalized SRS intensities of PS beads at various depths by PC-SRS and C-SRS. SRS intensities at different depths are normalized to the top layer (z=0) for better comparison. (**d**, **e**) SRS 3D images (2885 cm^{-1}) of porcine brain tissue acquired by PC-SRS and C-SRS. Scale bar: 20 μm. Image volume: 184.6 μm × 184.6 μm × 80 μm, with an axial step size of 8.8 μm. A total of 9 depths are imaged with a 1.5 s acquisition time per 3D volume. Average pump beam powers are 20 mW for PC-SRS and 4 mW for C-SRS, with a Stokes beam power of 45 mW on the porcine brain. (**f**) Comparison of SRS intensities at each tissue depth in porcine brain between PC-SRS and C-SRS. SRS intensities at each depth are normalized to the top-layer (z=0 μm) for performance comparison. (**g–i**) Dynamic SRS 3D images (2885 cm^{-1}) of 4.5 μm PS beads in water. Scale bar: 5 μm. Image volume: 23.08 μm × 23.08 μm × 16 μm, with an axial step size of 4 μm. A total of 4 depths are imaged with a 77 ms acquisition time per volume (13 Hz). Average powers of the pump and Stokes beams on the bead are 13 mW and 18 mW, respectively.

PC-SRS provides a ~2-fold improvement in penetration depth compared to C-SRS imaging, affirming its potential for deeper tissue 3D imaging.

We further demonstrate the efficacy of PC-SRS in enhancing penetration depth in biotissues (e.g., porcine brain tissue). Figure 3(d, e) present the SRS 3D images of porcine brain tissue captured by PC-SRS and C-SRS, revealing a higher SRS intensity from deeper tissue regions in PC-SRS. Figure 3(f) shows the normalized SRS intensity profiles of brain tissue along the depth z. Again, a significantly slower attenuation of SRS intensity in deeper brain tissue is observed by PC-SRS imaging compared to C-SRS. To quantitatively analyze the imaging depth by PC-SRS, we calculate the penetration depth of PC-SRS to be ~255.2 μm using an exponential decay function (refer to Section *Methods and materials*), giving a 2.5-fold improvement over C-SRS imaging (101.7 μm). Therefore, PC-SRS exhibits significantly enhanced penetration capability, facilitating deeper 3D chemical imaging in biotissues.

To illustrate the rapid 3D imaging capabilities of PC-SRS, we monitored the 3D Brownian motion of PS beads

in water. The sharp and artifact-free dynamic chemical images of the moving beads in water (Fig. 3(g–i)) can be acquired at a volume rate of 13 Hz (77 ms time interval) (see Media S1, Supplementary information for details) by PC-SRS, substantiating the capability of PC-SRS for rapid 3D chemical imaging.

Visualization of metabolic activitiy differences between tumor and normal zebrafish liver by PC-SRS

We apply the PC-SRS technique to visualize the metabolic progress differences between tumor and normal liver in living zebrafish models. Figure 4(a) and 4(b) show SRS 3D images of the zebrafish tumor liver from 6 to 11 dpf at 2935 cm^{-1} (CH_3 stretching of lipids and proteins) and 2186 cm^{-1} (CD bond), respectively. Figure 4(c) and 4(d) present SRS 3D images of zebrafish normal liver captured by PC-SRS at 2935 cm^{-1} and 2186 cm^{-1} over the same period for the comparison with (a, b) (details refer

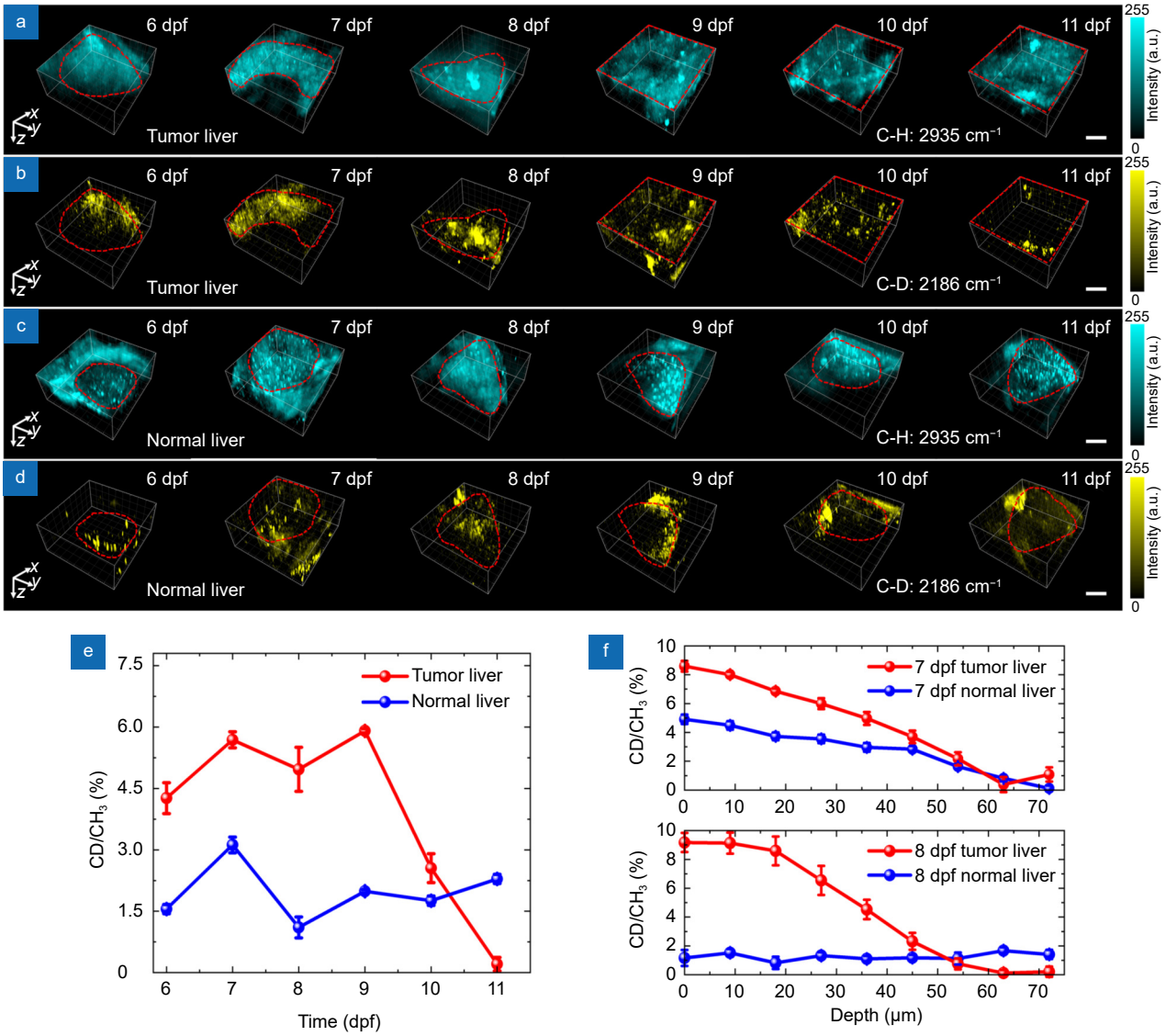

Fig. 4 | (**a**, **b**) SRS 3D images of tumor liver in zebrafish from 6 dpf to 11 dpf using PC-SRS (2935 cm^{-1}, CH_3 stretching of lipids and proteins, and 2186 cm^{-1}, CD bond). Image volume: 184 μm × 184 μm × 80 μm. Scale bar: 50 μm. (**c**, **d**) SRS 3D images of normal liver in zebrafish from 6 dpf to 11 dpf (2935 cm^{-1} and 2186 cm^{-1}), serving as normal control in comparison with (a, b). The regions surrounded by the red dotted lines represent the zebrafish liver acquired by PC-SRS. Image volume: 184 μm × 184 μm × 80 μm. Scalebar: 50 μm. The axial step size is 8.8 μm, with a total of 9 depths and a 15 s acquisition time for one 3D volume. Average laser powers were 20 mW at 797 nm and 25 mW at 848 nm, with a Stokes beam (1041 nm) power of 45 mW on the liver region. (**e**) Ratios of the volume-average SRS intensity at CD bond (2186 cm^{-1}) to CH_3 (2935 cm^{-1}) over time in both tumor and normal liver in zebrafish. (**f**) Ratios of the CD bond to CH_3 at various tissue depths in tumor and normal liver at 7 and 8 dpf.

to Media 2, Supplementary information). The regions of interest enclosed by the dotted red lines in (a-d) represent the liver areas within the PC-SRS 3D imaging volume at different time points. The tumor liver volume is much larger than that of the normal liver (especially after 9 dpf), reflecting a faster growth of tumor liver than normal liver.

To better visualize the metabolic activity differences between tumor and normal liver, we employed the ratio of CD (2186 cm^{-1}) to CH_3 (2935 cm^{-1}) as a metric for assessing D-element synthesis rate in liver (Fig. 4(e))[2,22,26]. PC-SRS shows that there is a 2- to 4-fold increase in D-element synthesis in the tumor liver compared to normal liver before 9 dpf, unveiling the upregulated metabolic activities in the tumor liver. However, the metabolic activity of the tumor liver significantly drops from 10 dpf to 11 dpf compared to that in normal liver, probably due to the approaching terminal phase of the tumor zebrafish's life cycle (all tumor zebrafish perished by 12 dpf). Furthermore, by leveraging the depth-resolved SRS imaigng capabilities of PC-SRS, we can monitor variations in metabolic activity across different tissue depths. Figure 4(f) shows the ratio of CD to CH_3 at various depths in 7 and 8 dpf zebrafish, where the volume sizes of tumor and normal liver are comparable, mitigating the impact of volume differences between the tumor and normal liver. The above results show that the liver tumor exhibits a much higher D-element synthesis near the liver surface compared to the normal liver. However, it shows a similarly slow metabolism in deeper liver regions. The observation unravels a higher metabolic activity occurring in the superficial layers of the liver tumor tissue, probably due to the relatively higher oxygenation and nutrients exchange rates from blood vessels in liver tumor tissue[27].

Multichannel 3D imaging of tumor and normal liver by PC-SRS

We have also employed PC-SRS to visualize the SRS intensities of lipids and proteins in the high wavenumber region in comparison with the CD bond in the cell-silent region. Figure 5(a) presents 3D image of a 7 dpf tumor liver using PC-SRS, where lipids and proteins are represented in green and red colors, respectively. Correspondingly, Fig. 5(b) shows the same 3D image volume of the tumor liver captured at 2186 cm^{-1} (CD bond). Figure 5(c, d) present the 3D volumes of normal liver obtained by PC-SRS for the comparison with the tumor liver in (a, b). Figure 5(e) displays SRS intensity ratios of the CD bond to both the lipids and proteins, respectively, as well as SRS ratios of lipids to proteins in both tumor and normal liver. Figure 5(f) depicts the results obtained by dividing the ratios in the tumor liver by those in the normal liver. We find that the incorporation of the CD bond ratio into the differentiation metrics yields approximately 2-fold enhancement in visualizing the metabolic activity differences between tumor and normal liver tissue compared to the use of the intrinsic cellular lipid and protein ratio alone.

Discussion

In this work, we developed a novel PC-SRS technique by electronically manipulating the shortened-length Bessel pump beam and the focused Gaussian Stokes beam simultaneously along the *z*-axis for rapid SRS 3D imaging in both cell-silent and high wavenumber regions without a need for mechanical *z*-scanning. In PC-SRS, a ring-shaped pump beam and a Gaussian Stokes beam are modulated at distinct areas of a single SLM, avoiding the dispersion effect induced by the SLM when simultaneously modulating the two large different wavelengths of light beams (i.e., pump beam of 800 nm, and Stokes beam of 1041 nm with 241 nm difference). The concentric distribution of phase patterns in PC-SRS not only facilitates easy operation for beam alignments, but also enables individual correction of system aberrations for both wavelengths. Further, after passing through the objective lens, the ring-shaped pump beam is transformed into a scattering-resilient Bessel pump beam in the sample. Combined with the use of a longer wavelength of Stokes beam (1041 nm in the NIR-II window[28]), PC-SRS achieves deeper tissue imaging in highly scattering media. For instance, compared to C-SRS imaging, we have experimentally demonstrated a ~2-fold improvement of imaging depth in PS beads phantom as well as ~2.5-fold improvement in brain tissue using PC-SRS (Fig. 3(a–f)). One notes that in C-SRS imaging, the significant wavelength difference (~240 nm) between the pump and Stokes beams may lead to the variation of system imaging aberrations for different wavelengths (Fig. 1(c, d)). Conventional aberration correction using a deformable mirror (DM) only provides a single correction phase when modulating both beams together[29], which may lead to an unbalanced correction, or in some cases, further deteriorate the system aberrations of the two beams used in SRS, consequently resulting in a lower SNR. In con-

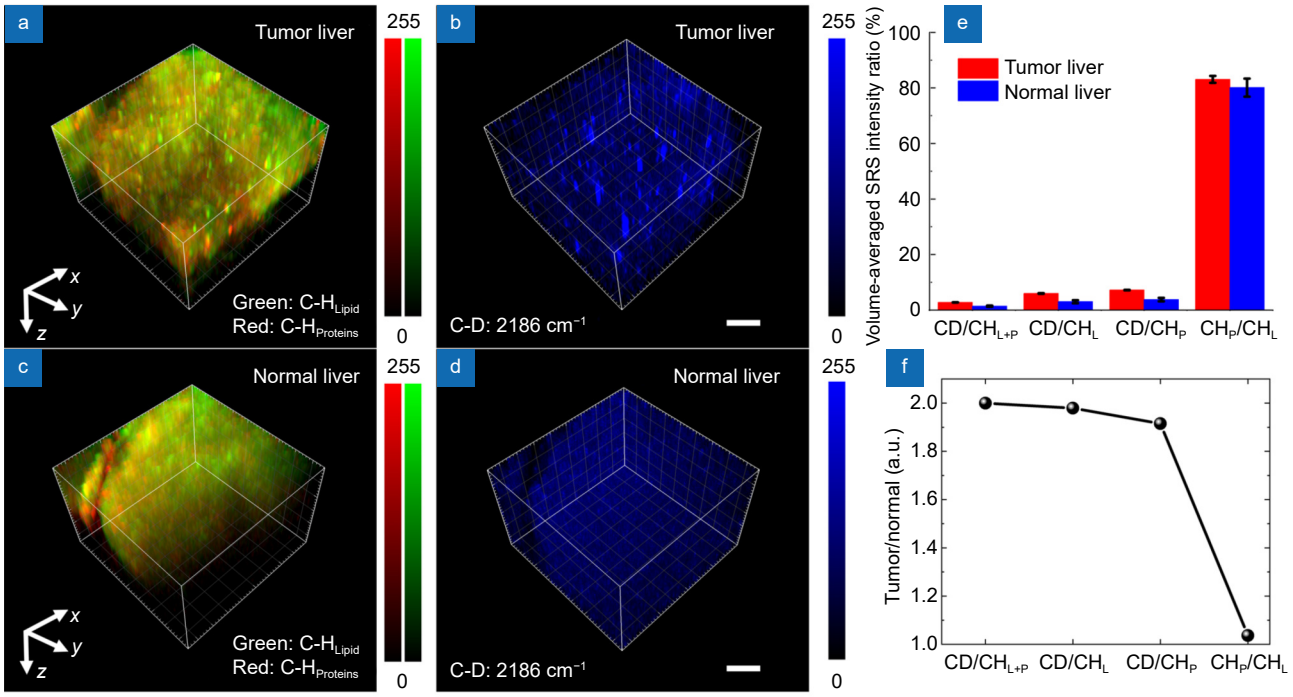

Fig. 5 | (**a**, **b**) SRS 3D images of tumor liver in living zebrafish (7 dpf) captured at 2935 cm^{-1} (CH_3 stretching of lipids and proteins), 2845 cm^{-1} (CH_2 symmetric stretching of lipids), and 2186 cm^{-1} (CD bond) using PC-SRS. The protein information is obtained by subtracting the 3D images at 2845 cm^{-1} from those at 2935 cm^{-1}. Image volume: 184 μm × 184 μm × 112 μm. Scale bar: 40 μm. (**c**, **d**) SRS 3D images of zebrafish normal liver (7 dpf) for the comparison with (a−b). Image volume: 184 μm × 184 μm × 112 μm. Scale bar: 40 μm. The axial step size is 8 μm, with a total of 14 depths and a 23 s acquisition time for one 3D volume. The average powers are 20 mW at 797 nm, 20 mW at 804 nm, and 25 mW at 848 nm, with a Stokes beam (1041 nm) power of 45 mW on the liver region. (**e**) Ratios of the volume-average CD bond intensity to CH intensity of lipids and proteins, as well as to lipids and proteins separately, in both tumor and normal liver. The ratio of CH_3 intensity of proteins to CH_2 intensity of lipids in both tumor and normal liver is also presented for comparison. (**f**) Comparison of the ratios of CD bond intensity to CH intensity versus the ratios of inherent CH_3 protein intensity to CH_2 lipid intensity between tumor and normal liver in zebrafish larvae.

trast, PC-SRS offers a significant advancement by enabling individual aberration correction for both the pump and Stokes beams (Fig. 1(c, d)) at various regions on the SLM plane, yielding a ~3-fold improvement in SNR for SRS imaging (Fig. 2(c)). The unique aberration correction scheme adopted in PC-SRS can be beneficial for further improving SNRs and the subsequent SRS deeper tissue imaging. In comparison with conventional deep tissue imaging methods, such as adaptive optics (AO) using a Shack-Hartmann wavefront sensor[30] or a wavefront reconstruction algorithm[31], PC-SRS enables deeper tissue imaging without the time delay accompanied with the wavefront detection, reconstruction, and compensation in AO, substantiating the robustness and versatility of PC-SRS for rapid SRS 3D imaging in deep tissue.

The PC-SRS technique developed in this work is fundamentally different from our previously reported phase-modulated (PM)-SRST imaging technique[23] in terms of their working principles, imaging system designs, and imaging performances. The unique imaging system designs in PC-SRS (e.g., the combination of ring-shaped pump beam and Gaussian Stokes beam, and the incorporation of Zernike polynomials (ZPs)) allow for the precise engineering of the Bessel beam's length and the corrections of the imaging system aberrations in both beams, which are challenging to accomplish by the PM-SRST technique. Compared to PM-SRST associated with the elongated Bessel beam designed (>100 μm)[23], PC-SRS coupled with a shortened-length Bessel pump beam (4.73 μm, FWHM, Supplementary information, Fig. S3) significantly increases the local laser excitation power density (>20-fold) with higher SNR for rapid SRS 3D imaging. Meanwhile, PC-SRS integrated with ZPs function corrections facilitates the image system aberrations for both pump and Stokes beams simultaneously, further improving SNRs of PC-SRS imaging (Fig. 2). Therefore, PC-SRS can achieve a much higher SNR than that in PM-SRST. Tapped on the high-SNR capability of PC-SRS associated with a fast electronic phase modulation

device (e.g., SLM), we have successfully demonstrated the utility of PC-SRS for rapid volumetric SRS imaging in cells and tissue imaging. For instance, the PC-SRS technique offers a significant improvement in imaging speed on millisecond scales (77 ms interval, 4 phase patterns, 13 Hz volume rate in Fig. 3(g–i)). Compared to PM-SRST, PC-SRS has a shorter 3D imaging acquisition time for a similar imaging volume (e.g., 2.3 s for PC-SRS (Fig. 3(a)), while 7.4 s is required for PM-SRST to image a 120 μm thick PS beads volume). To further boost the z-sectioning rates, a kHz micro-electromechanical system (MEMS)-based SLM or digital micromirror device (DMD)[32,33] could be employed in PC-SRS for modulating both the Bessel pump and Gaussian Stokes beams simultaneously, enabling video-rate SRS 3D imaging in tissue and cells. One notes that PC-SRS and PM-SRST share a similar capability of deeper 3D chemical imaging in tissues due to their use of the same excitation wavelenths of the Bessel pump beam (800 nm) and the NIR-II window Stokes beam (1041 nm) for SRS 3D imaging.

It is anticipated that the integration of shortened-length Bessel beam and ZPs used in PC-SRS with spontaneous Raman scattering effects could further advance the development of Raman tomography technique, providing a global identification of chemical and molecular characteristics in cells and tissue. Compared to projection Raman tomography[34] coupled with mechanical rotation stage, the phase-controlled technique could enable mechanical-scanning-free tomography with a rapid imaging capability. Compared to Raman tomography employed with the prolonged Bessel beating beams[35], PC-SRS method with shortened-length Bessel beam and ZPs achieves a higher local laser intensity, yielding a superior SNR for Raman tomography. Further, unlike diffuse optical tomography[36] with multiple scattering interference from other tissue depths on the millimeter resolution scale, PC-SRS with the use of scattering-resilient Bessel beams allows for deeper imaging in turbid tissue with sub-micron resolution.

Conclusions

We have developed a unique PC-SRS technique for rapid, deeper tissue SRS 3D imaging with high SNR at subcellular resolution. PC-SRS provides >2-fold improvement in imaging depth in a variety of samples (e.g., polystyrene bead phantoms, porcine brain tissue) as well as achieves SRS 3D imaging speed of ~13 Hz per volume for real-time monitoring of Brownian motion of polymer beads in water, superior to C-SRS 3D imaging. We also illustrate the utility of PC-SRS to monitor the metabolism changes of the entire tumor liver in living zebrafish with subcellular resolution in cell-silent region, unraveling the upregulated metabolism alterations in tumor liver in zebrafish larvae. One notes that the phase-controlled shortened-length Bessel beam focusing and aberrations correction method developed in PC-SRS is versatile, which can be readily adapted to other advanced microscopy techniques (e.g., CARS, harmonic generation, multiphoton, and fluorescence 3D imaging), enabling the rapid acquisition of morphological and biochemical information in cells and deep tissue. Therefore, the PC-SRS technique presented in this study holds a great promise for advancing the real-time monitoring of morphological and biochemical changes, metabolic and functional dynamic processes of live cells and tissue in biological and biomedical systems.

References

1. Bae K, Zheng W, Lin K et al. Epi-detected hyperspectral stimulated Raman scattering microscopy for label-free molecular subtyping of glioblastomas. *Anal Chem* **90**, 10249–10255 (2018).
2. Shi LY, Zheng CG, Shen YH et al. Optical imaging of metabolic dynamics in animals. *Nat Commun* **9**, 2995 (2018).
3. Bae K, Zheng W, Ma Y et al. Real-time monitoring of pharmacokinetics of mitochondria-targeting molecules in live cells with bioorthogonal hyperspectral stimulated Raman scattering microscopy. *Anal Chem* **92**, 740–748 (2020).
4. Lu FK, Basu S, Igras V et al. Label-free DNA imaging in vivo with stimulated Raman scattering microscopy. *Proc Natl Acad Sci USA* **112**, 11624–11629 (2015).
5. Wang Z, Zheng W, Hsu C Y S et al. Polarization-resolved hyperspectral stimulated Raman scattering microscopy for label-free biomolecular imaging of the tooth. *Appl Phys Lett* **108**, 033701 (2016).
6. Bae K, Zheng W, Huang ZW. Quantitative assessment of spinal cord injury using circularly polarized coherent anti-Stokes Raman scattering microscopy. *Appl Phys Lett* **111**, 063704 (2017).
7. Lin SL, Gong L, Huang ZW. Super - resolution two - photon fluorescence tomography through the phase - shifted optical beatings of bessel beams for high - resolution deeper tissue 3D imaging. *Laser Photonics Rev* **18**, 2300634 (2024).
8. Gong L, Zheng W, Ma Yet al. Higher-order coherent anti-Stokes Raman scattering microscopy realizes label-free super-resolution vibrational imaging. *Nat Photonics* **14**, 115–122 (2020).
9. Lin J, Lu FK, Zheng W et al. Assessment of liver steatosis and fibrosis in rats using integrated coherent anti-Stokes Raman scattering and multiphoton imaging technique. *J Biomed Opt* **16**, 116024 (2011).
10. Nandakumar P, Kovalev A, Volkmer A. Vibrational imaging based on stimulated Raman scattering microscopy. *New J Phys* **11**, 033026 (2009).
11. Wang Z, Zheng W, Huang ZW. Lock-in-detection-free line-scan stimulated Raman scattering microscopy for near video-rate Ra-

man imaging. *Opt Lett* **41**, 3960–3963 (2016).
12. Chapple PB, Staromlynska J, Hermann JA et al. Single-beam Z-Scan: measurement techniques and analysis. *J Nonlinear Opt Phys Mater* **6**, 251–293 (1997).
13. Wu JL, Ji N, Tsia KK. Speed scaling in multiphoton fluorescence microscopy. *Nat Photonics* **15**, 800–812 (2021).
14. Hill AH, Manifold B, Fu D. Tissue imaging depth limit of stimulated Raman scattering microscopy. *Biomed. Opt Express* **11**, 762–774 (2020).
15. Chen XL, Zhang C, Lin P et al. Volumetric chemical imaging by stimulated Raman projection microscopy and tomography. *Nat Commun* **8**, 15117 (2017).
16. Gong L, Lin SL, Huang ZW. Stimulated Raman scattering tomography enables label-free volumetric deep tissue imaging. *Laser Photonics Rev* **15**, 2100069 (2021).
17. Nussbaum A. Teaching of advanced geometric optics. *Appl Opt* **17**, 2128–2129 (1978).
18. Duocastella M, Arnold CB. Bessel and annular beams for materials processing. *Laser & Photonics Rev* **6**, 607–621 (2012).
19. Mahmoud MA, Shalaby MY, Khalil D. Propagation of Bessel beams generated using finite-width Durnin ring. *Appl Opt* **52**, 256–263 (2013).
20. Saidi IS, Jacques SL, Tittel FK. Mie and Rayleigh modeling of visible-light scattering in neonatal skin. *Appl Opt* **34**, 7410–7418 (1995)
21. Li HK, Li Y, Lu JW et al. Liver-specific androgen receptor knockout attenuates early liver tumor development in zebrafish. *Sci Rep* **9**, 10645 (2019).
22. Xin L, Huang MZ, Huang ZW. Quantitative assessment and monitoring of microplastics and nanoplastics distributions and lipid metabolism in live zebrafish using hyperspectral stimulated Raman scattering microscopy. *Environ Int* **187**, 108679 (2024).
23. Wang WQ, Huang ZW. Stimulated Raman scattering tomography for rapid three-dimensional chemical imaging of cells and tissue. *Adv Photonics* **6**, 026001 (2024).
24. Huang K, Ye HP, Teng JH et al. Optimization-free superoscillatory lens using phase and amplitude masks. *Laser Photonics Rev* **8**, 152–157 (2014).
25. Fahrbach FO, Rohrbach A. Propagation stability of self-reconstructing Bessel beams enables contrast-enhanced imaging in thick media. *Nat Commun* **3**, 632 (2012)
26. Xin L, Luo ZC, Liu XG et al. Unveiling the spatiotemporal and dose responses within a single live cancer cell to photoswitchable upconversion nanoparticle therapeutics using hybrid hyperspectral stimulated raman scattering and transient absorption microscopy. *Anal Chem* **96**, 6148–6157 (2024)
27. Vaupel P, Kallinowski F, Okunieff P. Blood flow, oxygen and nutrient supply, and metabolic microenvironment of human tumors: a review. *Cancer Res* **49**, 6449–6465 (1989).
28. Antaris AL, Chen H, Cheng K et al. A small-molecule dye for NIR-II imaging. *Nat Mater* **15**, 235–242 (2016).
29. Druon F, Chériaux G, Faure J et al. Wave-front correction of femtosecond terawatt lasers by deformable mirrors. *Opt Lett* **23**, 1043–1045 (1998).
30. Platt BC, Shack R. History and principles of Shack-Hartmann wavefront sensing. *J Refract Surg* **17**, S573–S577 (2001).
31. Ji N, Milkie DE, Betzig E. Adaptive optics via pupil segmentation for high-resolution imaging in biological tissues. *Nat Methods* **7**, 141–147 (2010).
32. Ersumo NT, Yalcin C, Antipa N et al. A micromirror array with annular partitioning for high-speed random-access axial focusing. *Light Sci Appl* **9**, 183 (2020).
33. Geng Q, Gu CL, Cheng JY et al. Digital micromirror device-based two-photon microscopy for three-dimensional and random-access imaging. *Optica* **4**, 674–677 (2017).
34. Wang N, Wang XY, Yan TY et al. Label-free structural and functional volumetric imaging by dual-modality optical-Raman projection tomography. *Sci Adv* **9**, eadf3504 (2023).
35. Shu C, Gong L, Huang ZW. Bessel beam beating-based spontaneous Raman tomography enables high-contrast deep tissue Raman measurements. *ACS Photonics* **11**, 2022–2034 (2024).
36. Demers JLH, Esmonde-White FWL, Esmonde-White KA et al. Next-generation Raman tomography instrument for non-invasive *in vivo* bone imaging. *Biomed Opt Express* **6**, 793–806 (2015).

Acknowledgements

This work was supported by the Academic Research Fund (AcRF) from the Ministry of Education (MOE) (Tier 2 (A-8000117-01-00) and Tier 1 (R397-000-334-114, R397-000-371-114, and R397-000-378-114)), 2024 Tsinghua-NUS Joint Research Initiative Fund, and the National Medical Research Council (NMRC) (A-0009502-01-00, and A-8001143-00-00), Singapore.

Author contributions

Z. W. Huang conceived the concept and supervised the project. W. Q. Wang built the system and performed the measurements and data curations. Z. W. Huang and W. Q. Wang involved in data analysis and drafting manuscript. Z. W. Huang finalized the manuscript.

Competing interests

The authors declare no competing financial interests.

Supplementary information

Supplementary information for this paper is available at https://doi.org/10.29026/oea.2024.240064